ACS OMEGA

http://pubs.acs.org/journal/acsodf
Article

Fabrication of the Fe-Doped Corona Schiff Base for Enhanced Microwave Absorption Performance

Jun Li, Yuhang Hua, Qiannan Yuan, Wenqi Gou, Hao Sun, Long Lin, Mengtao Wang, Mingxun Yu, and Aiwen Qin*

Cite This: *ACS Omega* 2023, 8, 38885−38894
Read Online
ACCESS | Metrics & More | Article Recommendations

ABSTRACT: A corolla-shaped Schiff base polymer was synthesized from terephthalaldehyde (TPAD), glutaraldehyde (GA), and *p*-phenylenediamine (PPD) by block copolymerization, and Schiff base iron complexes were formed by doping with $FeCl_3$. The microscopic morphology, crystal structure, and elemental valence state were characterized by field emission scanning electron microscopy (FESEM), Fourier transform infrared spectroscopy (FTIR), X-ray diffraction (XRD), and X-ray photoelectron spectroscopy (XPS). Comparing the change of conductivity before and after Fe^{3+} doping, it was found that the conductivity did not break away from the category of insulator, and the doped sample is a paramagnetic material. Morphological changes were observed by adjusting the ratio of GA to TPAD, and it was found that the corolla-like structure was most complete when the ratio of GA to TPAD was 2:1, and its Schiff base iron complex absorbed waves better. At a thickness of 3 mm, the absorption effect can reach below −10 dB at 12.44−15.16 GHz, and the maximum absorption value is −45.07 dB at a thickness of 3.8 mm; it is an organic absorbing agent with excellent impedance matching and absorbing properties.

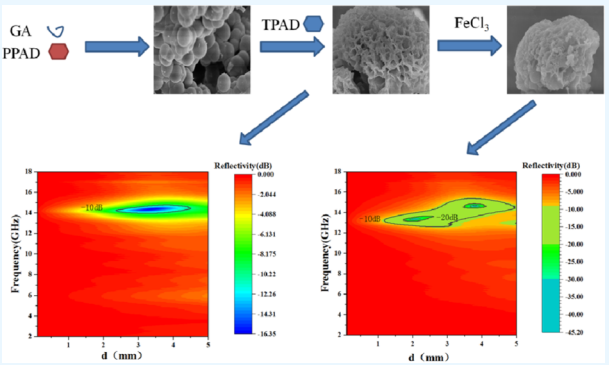

1. INTRODUCTION

With the development of 5G technology, smart home, smart wearable, smart city, and driverless will be quietly integrated into our lives. Radio waves have been greatly enriched and developed, touching every aspect of our lives, providing us with convenience, but also leaving a lot of electromagnetic pollution.[1−4] Electromagnetic pollution not only threatens human health but also interferes with the normal operation of machines, so absorbing materials has attracted people's attention.[5−7] An absorbing material refers to a material that can absorb and attenuate the energy of incident electromagnetic waves and convert electromagnetic energy into heat energy dissipation or disappearance.[8] The ideal absorbing material should have the characteristics of "lightweight, thin thickness, wide absorption band, and strong absorption peak." In recent years, the Schiff base has been widely used in the development of new materials due to its mild and simple reaction conditions, single reaction products, and dynamic reversible reaction characteristics.[9−11] It has been reported that the Schiff base can improve its conductivity and electromagnetic properties by doping with metal ions,[12−14] so it is a kind of wave-absorbing material with good characteristics.

Zhao et al. explored the electromagnetic properties of the PPD-benzaldehyde Schiff base silver complex grown on graphene with an intercalation structure. It was found that its conductivity was 5.07 S/cm, saturation magnetization was 2.93 emu/g, residual magnetization was 0.69 emu/g, and coercive force was 104.68 Oe.[15] Hassib et al. studied the dielectric and electrical conductivity of 5,7-dihydroxy-6-formyl-2-tolyl-4-ketal ethylenediamine Schiff bases in different temperature ranges (300 K < T < 420 K) and frequency ranges (0.1−20 kHz). When T > 350 K, the dielectric loss rate would decrease with the increase in temperature and frequency.[16] Courric et al. studied the conductivity and electromagnetic properties of composite materials, which were obtained by adding a Schiff base-conjugated polymer into PVC and doping with H_2SO_4. The conductivity of composite materials was 10^{-5} ∼ 10 S/cm (10 kHz to 10 GHz), and it was found that the reflectance of composite materials with different thicknesses fluctuates in the range of −9 to −20 dB.[17] The Schiff base, as an organic conductive polymer, the conductivity, and magnetic energy are far less than those of inorganic matter, whose intrinsic conductivity is generally

Received: April 29, 2023
Accepted: October 4, 2023
Published: October 16, 2023

10^{-9}−10^{-8} S/m.[18] However, its conductivity can reach the level of semiconductors after doping or complexing with metal ions and transform from a diamagnetic substance to a paramagnetic substance.[19] This kind of material also has the advantages of low density, good compatibility, adjustable electromagnetic parameters, easy composite processing, and industrial production.[20,21]

Most researchers improve its wave-absorbing effect by compounding it with carbon materials, and the effect is significant.[22,23] It is worth noting that the excellent absorbing performance of this composite material is mainly provided by the strong dielectric loss capability of the carbon-based material itself, and the loss capability of the Schiff base absorber is not strong. For example, the Ag−Schiff base/rGO composite studied by Xu et al. can reach an effective absorption bandwidth of 6.28 GHz.[24] While the minimum absorption peak of the Ag−Schiff base complex is −3.23 dB, with no effective absorption bandwidth. The effective absorption bandwidth of 3D-rGA is 5.8 GHz, and the minimum absorption value is −35.79 dB. It can be seen that the excellent absorption performance is mainly provided by 3D-rGA. Therefore, from the perspective of enhancing the loss ability of organic absorbers, this article assembled two different types of Schiff bases to prepare corolla Schiff bases and explored the impact of changes in morphology on the absorbing performance.

Based on the spherical Schiff bases[18] and lamella Schiff bases[19] previously studied, a corolla Schiff base with wave-absorbing properties was developed in this paper. TPAD and GA were copolymerized with PPD to form a block copolymer, and the ratio of TPAD and GA was adjusted to observe the morphology changes. Through a coordination reaction, Fe^{3+} can react with the Schiff base C═N bond, the lone pair electron of nitrogen atoms in the poly(Schiff bases) complexes is an electron donor, and the coordinated metal ion is an electron acceptor. On the one hand, the coordination reaction expands the movement range of electrons, allowing electrons to move at lower energies, and dielectric loss can occur under electromagnetic wave irradiation. On the other hand, when Fe^{3+} is combined with the Schiff base, the material has a certain weak magnetism. When electromagnetic waves are irradiated on the material, magnetic loss can also occur. Under the double loss of electricity and magnetism, the Schiff base can quickly convert electromagnetic energy into heat energy and disperse it. By testing electromagnetic parameters, the absorbing mechanism of the corolla Schiff base was explored, and beneficial exploration was made for its further application.

2. EXPERIMENTAL SECTION

2.1. Experimental Reagents and Instruments. GA, PPD, and anhydrous ethanol were purchased from Tianjin Comiou Chemical Reagent Co., Ltd. TPAD and anhydrous ferric chloride were purchased from Aladdin Chemical Reagent Co., Ltd. All reagents were analytically pure without further treatment before the experiment.

A FW-5 Powder Tablet Press, Tianjin Botian Shengda Technology Development Co., Ltd.; a WinCHEM2.05 Dielectric spectrometer, GmbH&Co. KG Company; a Tensor-37 Fourier transform infrared spectrometer, Bruker; a Quanta-200 Scanning Electron Microscope, PEI Company; an X-ray diffractometer, Bruker; and an X-ray photoelectron spectroscope, EDAX Inc were used.

2.2. Preparation of the Corolla Poly-Schiff Base (C1). The preparation steps are as follows: (1) 3.27 g (0.03 mol) of PPD was added to a 250 mL three-mouth flask, then 70 mL of anhydrous ethanol was added, and the magnetic stirring was performed evenly. (2) 3.86 mL (0.02 mol) of GA was dissolved in 20 mL of anhydrous ethanol, slowly dripped into three flasks through a constant pressure buret, and cooled and refluxed for 4 h in a constant temperature water bath at 80 °C. (3) 1.34 g (0.01 mol) of TPAD was completely dissolved in 30 mL of absolute ethanol and slowly dropped into the three-necked flask through a constant pressure buret to continue the reaction for 6 h. (4) The resulting orange-yellow precipitate was vacuumed and filtered, washed with anhydrous ethanol three times, and finally dried in a vacuum oven at 80 °C.

2.3. Preparation of Corolla Poly-Schiff Bases Doped with $FeCl_3$ (C2). 0.003 mol (0.486 g) $FeCl_3$ was completely dissolved in 60 mL of anhydrous ethanol and was added to the flask containing 20 mL of anhydrous ethanol and 0.646 g (0.001 mol) of a petal-like poly-Schiff base (C1) with a constant pressure funnel. The flask was reflowed at 80 °C and magnetically stirred for 4 h, and then vacuum filtrated and cleaned with anhydrous ethanol 3 times. The black solid Schiff base iron complex was prepared by vacuum oven drying at 80 °C. The preparation process of C2 is illustrated in Figure 1.

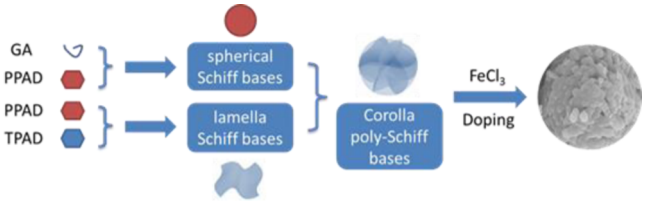

Figure 1. Synthesis process for corolla poly-Schiff bases doped with $FeCl_3$ (C2).

2.4. Conductivity Test. A circular sheet with a diameter of 12 mm and a thickness of less than 1 mm was prepared by a powder tableting machine. The sample preparation pressure and holding time were 10 MPa and 2 min, respectively. Then, the electrical conductivity of the pressed circular sheet was measured at room temperature by a WinCHEM2.05 dielectric spectrometer of GmbH & Co. KG.

2.5. Complex Permeability and Complex Permittivity Tests. An Agilent 8722ES microwave vector network analyzer was used to test the four electromagnetic parameters of the relative dielectric constant and relative permeability in the frequency range of 2−18 GHz, with a step length of 0.02 GHz. A coaxial ring sample with an outer diameter of 7.0 mm and an inner diameter of 3.0 mm was prepared by mixing Schiff base powder with paraffin at a mass ratio of 1:3. Electromagnetic absorption performance was calculated with the following formulas[25,26]

$$\mathrm{RL} = 20 \log \left| \frac{z_{\mathrm{in}} - z_0}{z_{\mathrm{in}} + z_0} \right| \tag{1}$$

$$Z_{\mathrm{in}} = Z_0 \sqrt{\frac{\mu_{\mathrm{r}}}{\varepsilon_{\mathrm{r}}}} \tanh\left[\left(j \frac{2\pi f d}{c} \right) \sqrt{\mu_{\mathrm{r}} \varepsilon_{\mathrm{r}}} \right] \tag{2}$$

$$Z_0 = \sqrt{\frac{\mu_0}{\varepsilon_0}} \tag{3}$$

https://doi.org/10.1021/acsomega.3c02956
ACS Omega 2023, 8, 38885−38894

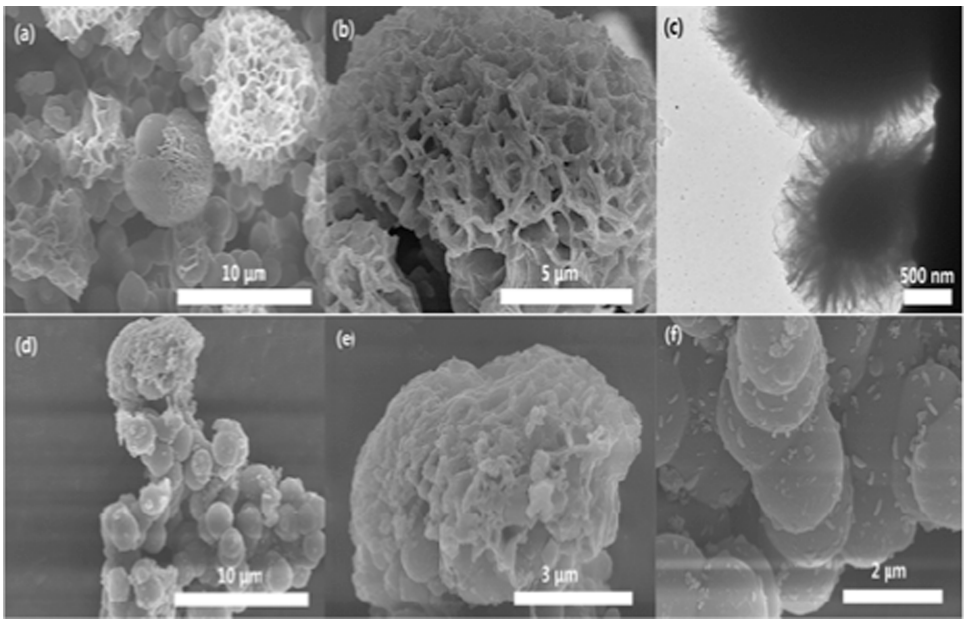

Figure 2. Scanning electron microscopy (SEM) images of C1 (a, b) and C2 (d–f) and TEM images of C1 (c).

Z_0 and Z_{in} are the free impedance of space and the normalized input impedance of the material, respectively, C is the speed of light, d is the thickness of the sample, and f is the microwave frequency, μ_0 and ε_0 are the complex permeability and complex dielectric constant in free space, respectively, and μ_r and ε_r are the complex permeability and complex dielectric constant of the material, respectively.[27]

3. RESULTS AND DISCUSSION

It can be seen that C1 has a corolla structure (Figure 2b). Through transmission electron microscopy, there are spherical Schiff base particles in the middle and surrounded by lamellar Schiff base lamellas (Figure 2c). Figure 2a shows the overall morphology of C1. It can be seen that C1 is formed by the three-dimensional accumulation of spherical Schiff bases. The surface of the stacked spheres is wrapped with sheet-like Schiff base single crystals, forming a petal-like structure. As the petals grow, spherical particles will be wrapped inside, as shown in Figure 2c. The overall morphology of the Schiff base after doping with $FeCl_3$ does not change much (Figure 2d). The porous structure on the petals disappears after doping, and the whole is adhered together. The surface of the granular Schiff base appears to have randomly distributed bumps (Figure 2e). The petal-like Schiff base has a strong anisotropy, and this anisotropy contributes to both its dielectric and magnetic losses.

Figure 3 shows the infrared spectra of C1 and C2. Since C1 and C2 are polymers with constantly repeating structural units, some characteristic peaks are strengthened. For example, the characteristic peak around 3123 cm^{-1} is caused by the stretching vibration of C−H on unsaturated carbon (double bond and benzene ring). The characteristic peak at 820 cm^{-1} is caused by the out-of-plane bending vibration of −CH on the aldehyde group. The characteristic peak at 620 cm^{-1} is caused by the out-of-plane bending vibration of −CH, where the benzene ring is substituted. The stretching vibration of the characteristic peak C═N of the Schiff base reaches 1624 cm^{-1}.[28,29] The absorption peaks of symmetric and antisymmetric stretching vibrations of the primary amine N−H bond

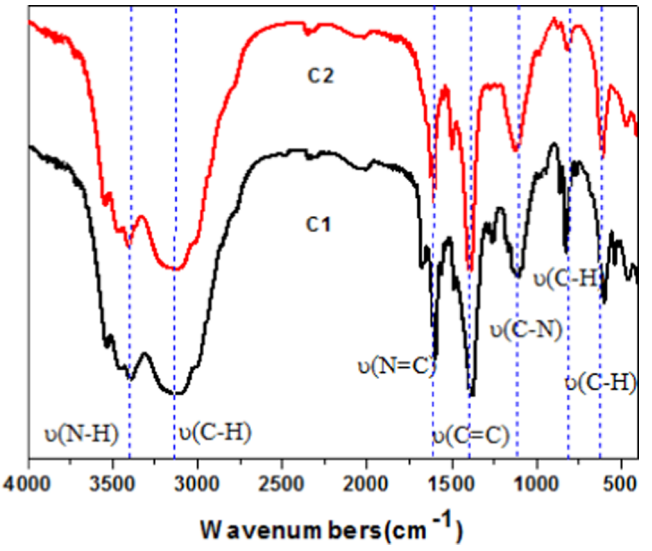

Figure 3. Fourier transform infrared (FTIR) spectra of C1 and C2.

are located near 3421 cm^{-1}. The absorption peaks at 1401 and 1124 cm^{-1} are the characteristic absorption peaks of the skeletal bending motion of the C═C bond of the benzene ring and the stretching motion of the aromatic C−N bond, respectively.

Figure 4 shows the X-ray diffraction (XRD) crystal curves of C1 and C2. The top three peaks of C1 mainly appear at 2θ = 20.7, 30.1, and 38.3°. The absorption peak at 20.7° is the characteristic peak of the lamellar petal crystal.[19] The characteristic diffraction peaks of C2 are 2θ = 14.1, 16.4, 26.5, and 35.2°. Due to the fluorescence effect of Fe^{3+}, the XRD curve of C2 has many impurity peaks and a high baseline; only a few small sharp peaks can be identified. So far, there is no report to determine the crystal forms of C1 and C2.

Figure 5 shows the X-ray photoelectron spectroscopy (XPS) curve of C2. Its main constituent elements are C, N, O, Fe, and Cl. From the inset to determine the valence states of iron ions in the sample, it can be seen that the binding energies of Fe

https://doi.org/10.1021/acsomega.3c02956
ACS Omega 2023, 8, 38885−38894

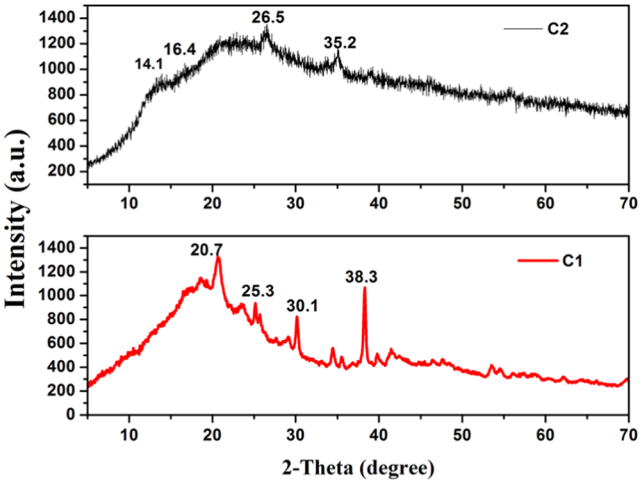

Figure 4. XRD patterns of C1 and C2.

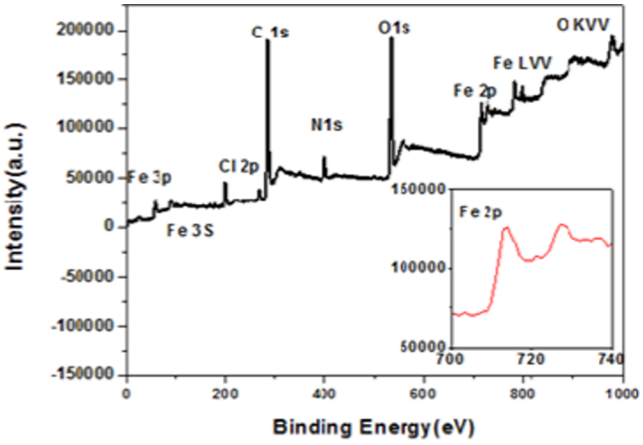

Figure 5. XPS patterns of C1 and C2.

$2p_{2/3}$ and Fe $2p_{1/2}$ of C2 are 713.4 and 727.1 eV, respectively. There is also a satellite peak at 719.08 eV, and the characteristic peak at 719 eV is the typical binding energy peak of Fe^{3+} in γ-Fe_2O_3,[30] indicating that the iron ion in C2 exists in a positive trivalent state.

Iron-doped materials often have intriguing magnetic properties because the structure, shape anisotropy, and crystallographic orientations can evidently influence the magnetic properties of microstructured and nanostructured materials.[31] The magnetic properties of C2 were examined by a SQUID magnetometer at 300 K with a magnetic field in a range of −2 T Oe < H < 2 T Oe. Figure 6 is a diagram of the hysteresis loop of C2. The maximum magnetization of C2 is 0.17 emu/g, and its coercive force H_C and residual magnetization M_r are 48.28 Oe and 0.000661 emu/g, respectively. Moreover, when the electron of the N atom jumps into the 3s orbit of Fe^{3+}, the magnetic moment will be formed. It can be seen from the diagram that C2 is a paramagnetic material with weak magnetism, which is consistent with the result of the literature.[16,32]

From the morphology and preparation process of C2, it is clear that the coronal Schiff base is self-assembled from spherical and lamellar Schiff bases through intermolecular forces. It is a spherical Schiff base formed by the polycondensation of GA and PPD as the core and a lamellar Schiff base formed by PPD and TPAD as the petals. To further

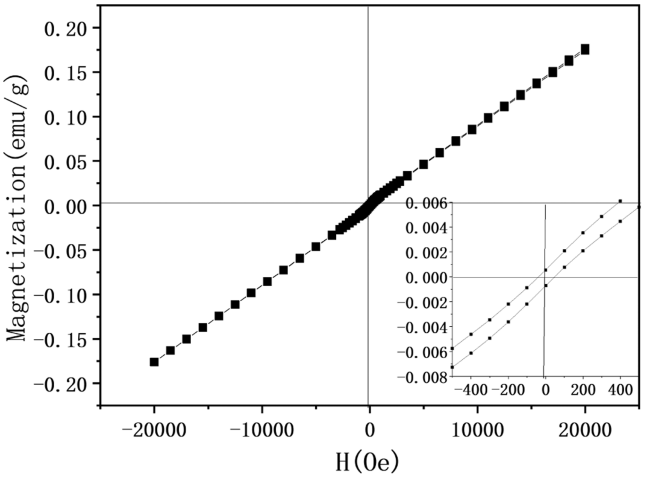

Figure 6. Magnetic hysteresis loop of C2.

understand the effect of different ratios of GA and TPAD on the morphology of Schiff bases, C3, C4, C5, and C6 were synthesized by reacting GA and TPAD in proportions of 1:1, 3:1, 1:2, and 3:1 with PPD in the steps described in 2.2.

Figure 7a shows the morphology of C3, where it can be seen that part of it is a smooth spherical poly-Schiff base, and the

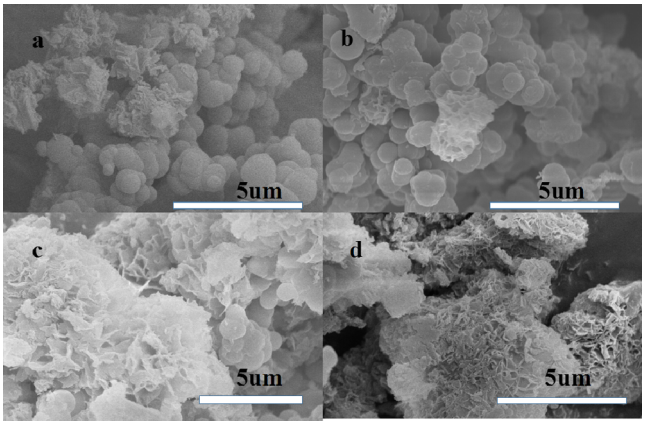

Figure 7. FESEM images of C3 (a), C4 (b), C5 (c), and C6 (d).

other part of the spherical is full of lamellar crystals. Although these crystals form a crown-like structure, the lamellar crystals are more random and cannot form an orderly petal-like shape. Figure 7b shows a photograph of C4, which has a high proportion of GA during the synthesis process, so its photograph is basically all spherical Schiff base particles, with only a few scattered particles with corolla-like structures on top. The field emission SEM (FESEM) photograph of C5 is shown in Figure 7c; corolla-like structures increased and gradually joined together, and there are a few spherical Schiff base particles with smooth surfaces. C6 is the Schiff base copolymer with the highest percentage of TPAD, resulting in its photo with a basically blocky structure, with lamella crystals growing on the surface of the spherical structure and lamella Schiff bases connected with each other and wrapped around the whole spherical Schiff base. When the ratio of TPAD to GA is greater than 3:1, the corolla-like structure disappears, and the lamella crystals are connected to form a block. When the ratio is less than 1:3, the copolymer Schiff bases appear granular.

https://doi.org/10.1021/acsomega.3c02956
ACS Omega 2023, 8, 38885−38894

Figure 8 illustrates the conductivity of all polymers increases with increasing frequency, and the maximum value is 5.56 × 10^{-5} S/cm reached at 1 × 10^{7} Hz, indicating that the doping of Fe^{3+} and the change of structural anisotropy have little effect on the conductivity, and the copolymer Schiff base is basically not out of the insulator. In the range of 1.8 × 10^{5} ∼ 2.0 × 10^{6} Hz, a resonance peak appears in this range and should have good dielectric relaxation.

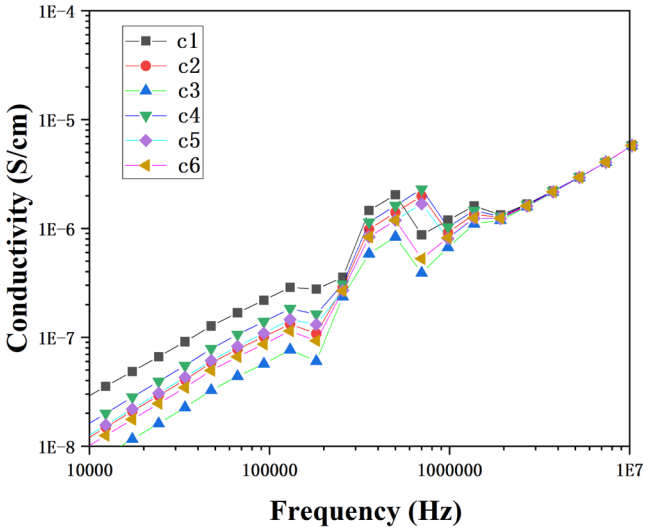

Figure 8. Curves of conductivity with frequency for C1, C2, C3, C4, C5, and C6.

The absorption characterization parameters of C2, C3, C4, C5, C6, and C2 were measured with an Agilent Vector Network Analyzer, and the results are shown in Figure 9. As can be seen from Figure 9a, the real part of the complex dielectric constant ε' of the six samples decreases slowly with the increase of frequency in 2−18 GHz. The ε' of C1, C3, C4, C5, C6, and C2 decreased from 2.43, 2.94, 2.31, 2.64, 2.27, and 2.76 to 2.32, 2.52, 2.24, 2.52, 2.18, and 2.62, respectively. In addition, the ε' of C3 is the largest among the six samples in the range of 2−14 GHz, and the ε' C2 exceeds C3 in the range of 14−18 GHz. As shown in Figure 9c, the imaginary part of the complex dielectric constant ε'' has a peak value at 1.07−1.67 GHz, and the peak value of C3 is the maximum value of six samples, which can reach 0.56. Dielectric loss peaks of C2 and C1 also appear; the peaks were 0.23 and 0.28. The dielectric loss tangent $\varepsilon''/\varepsilon'$ of the sample is shown in Figure 9e; the trend of $\varepsilon''/\varepsilon'$ is the same as ε'', and only the peak values are different. To sum up, C3 has the most outstanding dielectric loss capacity.

Dielectric polarization of six kinds of Schiff base materials is mainly caused by molecular polarization and molecular relaxation.[33] Under the action of an alternating electro-

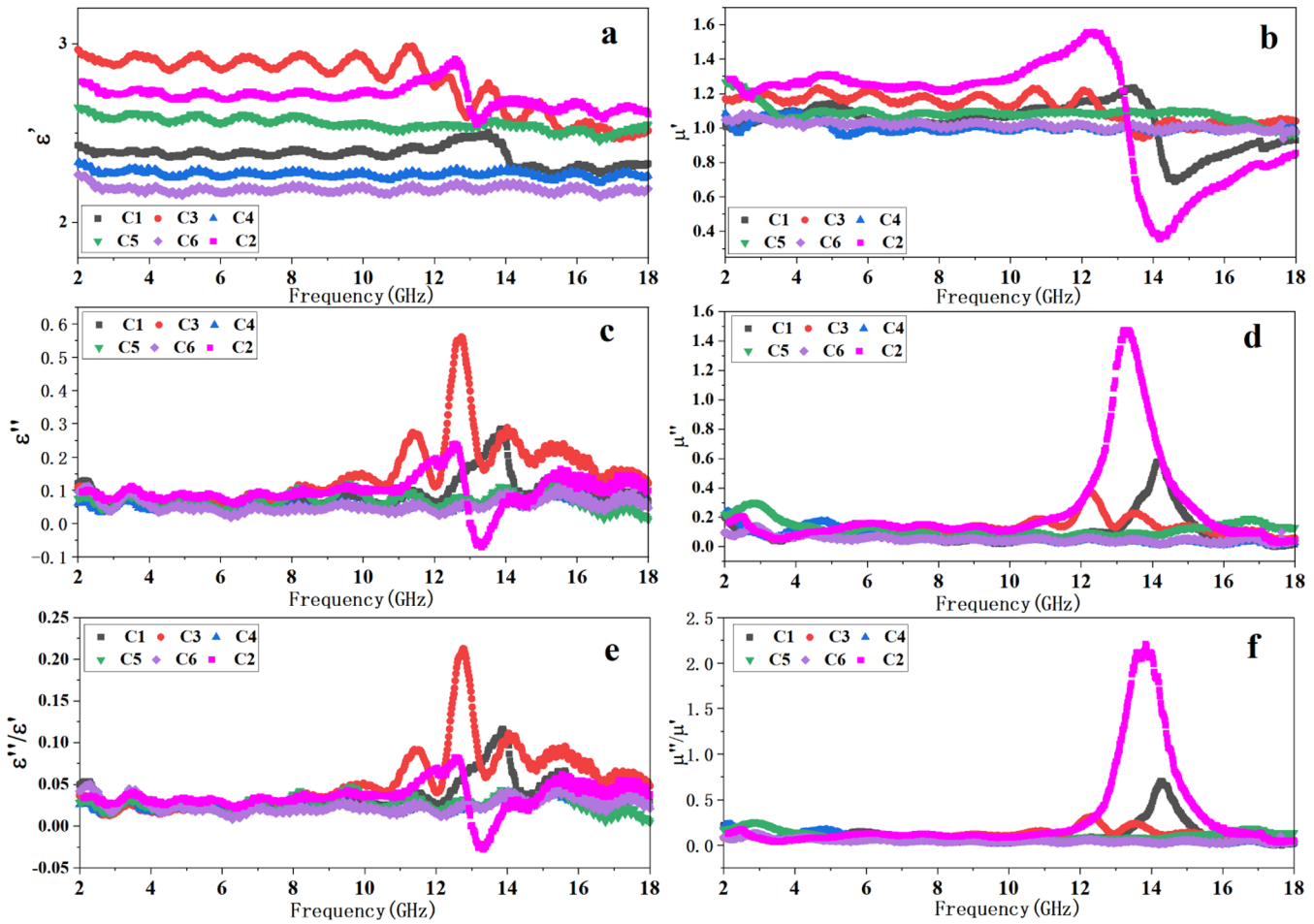

Figure 9. Real part of complex permittivity (a); imaginary part of complex permittivity (b); dielectric loss tangent (c); real part of complex permeability (d); imaginary part of complex permeability (e); and magnetic loss tangent of C1, C3, C4, C5, C6, and C2 with frequency.

https://doi.org/10.1021/acsomega.3c02956
ACS Omega 2023, 8, 38885−38894

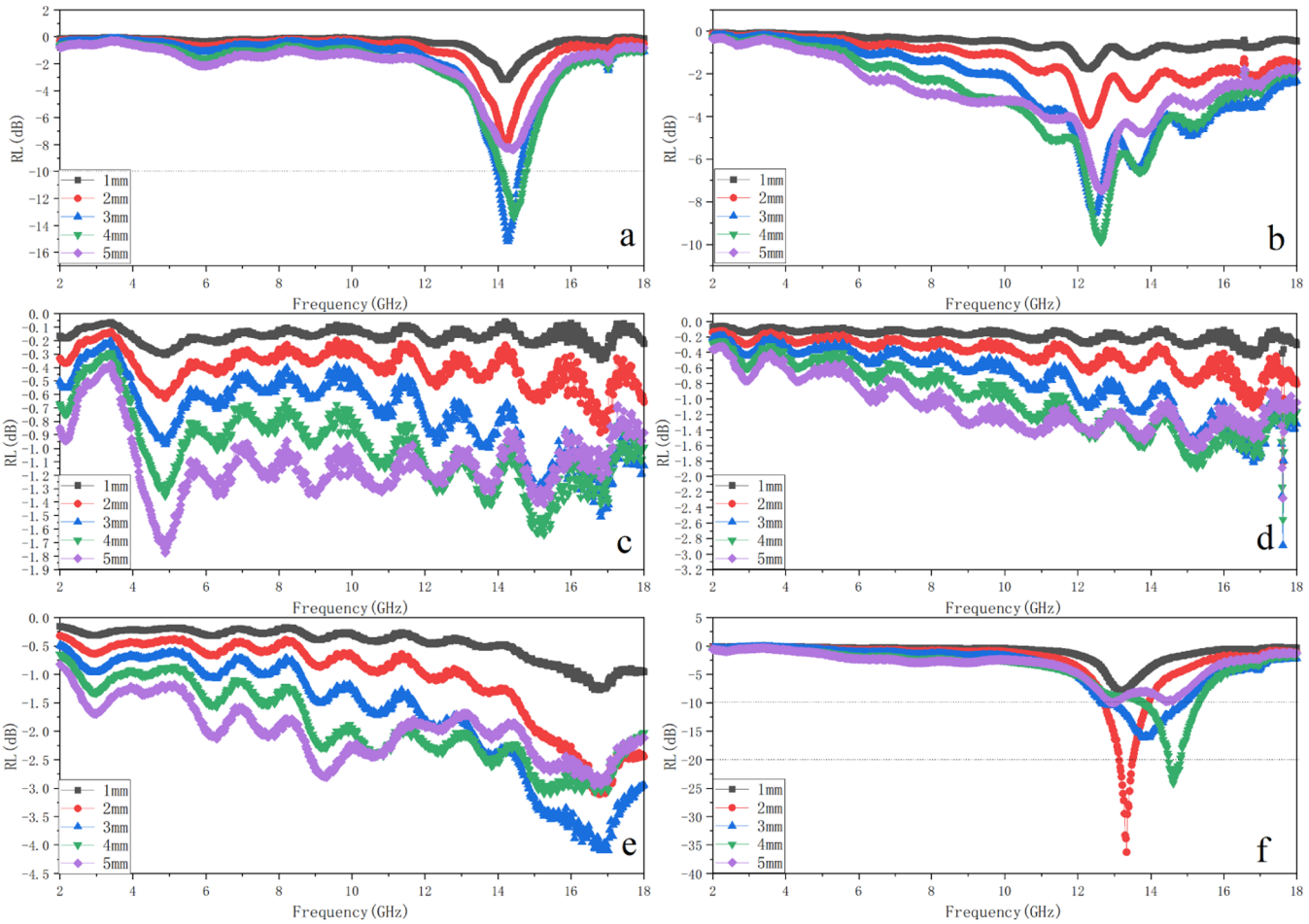

Figure 10. Reflectivity curves of C1 (a), C3 (b), C4 (c), C5 (d), C6 (e), and C2 (f) in the thickness d = 1, 2, 3, 4, and 5 mm.

magnetic field, the molecular orientation rotation occurs, and polar molecules are disoriented by thermal motion, which forms a molecular relaxation process and results in energy loss in friction and collision.[34−36] From the electron micrograph of 6A, it can be seen that C3 mainly has a large number of spherical particles, which are more easily poled in an alternating electric field than the sheet Schiff base; therefore, C3 has a higher dielectric poling ability. For C2, in addition to molecular polarization and molecular relaxation, dipole polarization also contributes to dielectric loss. The polarized metal can act as a dipole during the dipole polarization, and the phenomenon is particularly prominent in the high-frequency band; this phenomenon has been confirmed.[37] For this experiment, a series of Schiff bases were synthesized, and after doping with excess $FeCl_3$, some Fe^{3+} was adsorbed on the surface of Schiff bases and oxidized by air to generate Fe_2O_3, which is consistent with the XPS detection. Fe_2O_3 acts as a dipole in the Schiff base polarization process coupled with the interaction of the intrinsic dipole of the corolla Schiff base, resulting in an obvious dielectric polarization in the high-frequency region.

Permeability (μ) represents the magnetic loss capacity of an absorber.[38] Figure 9d shows the real part of the complex magnetic loss μ' of six samples. It can be seen that the values of C4, C5, and C6 are basically stable at around 1.0 in the whole range, and only the samples C1, C2, and C3 have peaks. The permittivity of sample C3 oscillates slightly at 2−14 GHz and decreases gradually at 14−18 GHz. C1 has a maximum value of 1.24 at 13.6 GHz and a minimum value of 0.68 at 1.46 GHz. C2 has a maximum value of 1.55 at 12.33 GHz and a minimum value of 0.36 at 14.23 GHz. It can be seen that the permeability of C2 increases greatly after complexing with Fe^{3+}, and it has a strong ability to store magnetic energy. Figure 9e shows the variation of the imaginary part μ'' of the complex permeability of six samples with frequency, which is similar to μ'. Only C1, C2, and C3 had maximum values, which were 0.58,1.47, 0.36 at 14.16 GHz, 13.3 GHz, and 12.2 GHz, respectively. The magnetic loss tangent μ''/μ' of the sample is shown in Figure 9e. The trend of μ''/μ' is the same as μ'', and only the peak values are different. In a word, C2 has the most outstanding magnetic loss capacity.

The magnetic loss capacity included natural resonance and exchange resonance.[39] The natural resonance results from shape anisotropy and magnetocrystalline anisotropy,[40] while the exchange resonance originates from the surface anisotropy and exchange energy between grains.[41] The corolla Schiff bases have an increased magnetic anisotropy due to their large shape anisotropy. This three-dimensional structure is assembled from nanosecondary structures, which are affected by the secondary structure. The lamella Schiff base secondary structure has strong anisotropy due to the different aspect ratios. The frequency of natural resonance is proportional to the anisotropy of the material, which means that the greater the anisotropy, the higher the resonance frequency.[42] Therefore, the magnetic loss tangent value of the sample is shifted to the high-frequency region. Because of its low electrical con-

https://doi.org/10.1021/acsomega.3c02956
ACS Omega 2023, 8, 38885−38894

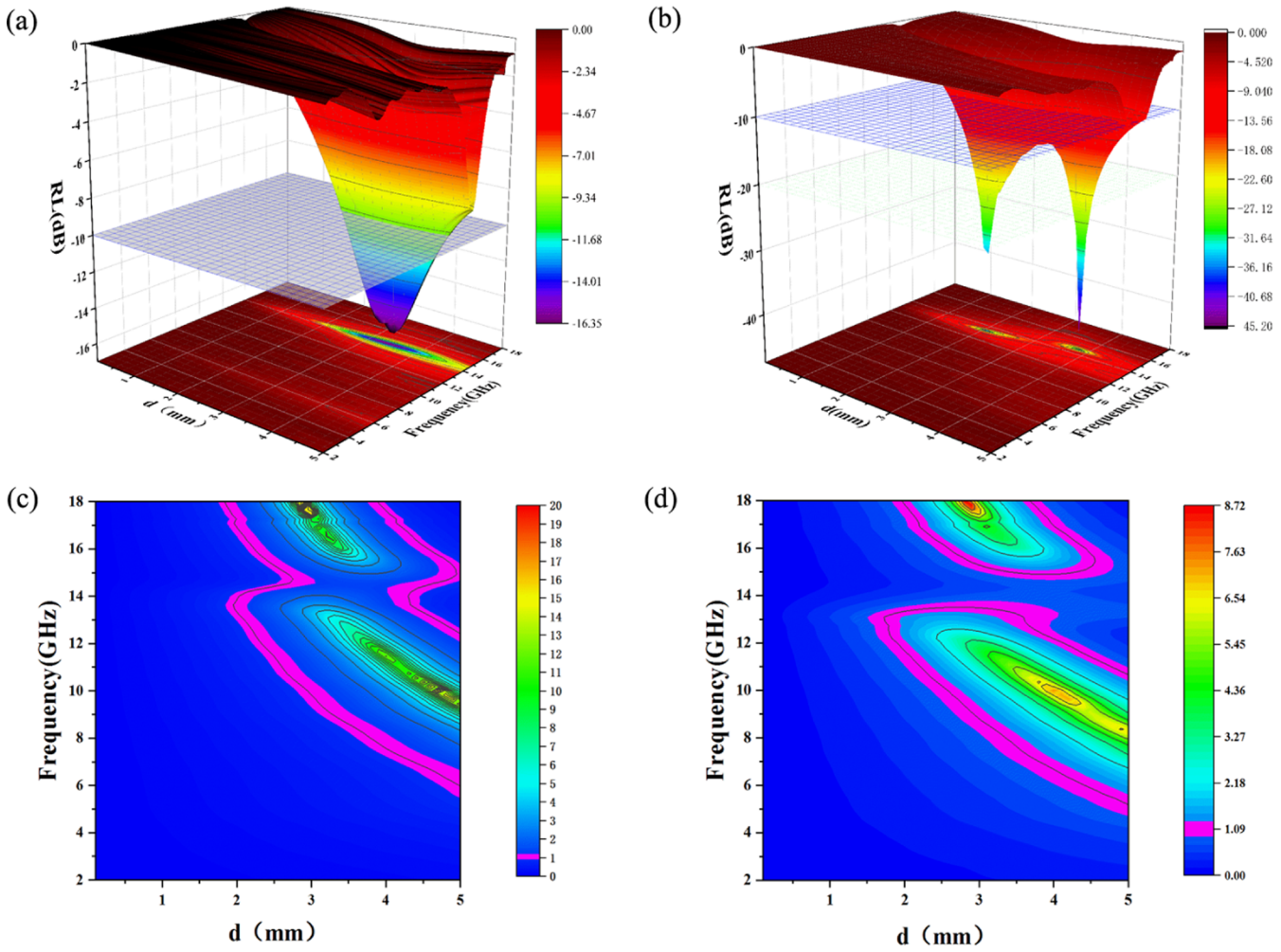

Figure 11. Reflectivity 3D plots (a, b) and matching parameter Z values 3D plots (c, d) of C1, C2.

ductivity, the corolla Schiff base cannot form current under the action of an alternating electric field, so eddy current loss can be ignored. In conclusion, the hysteresis loss of the sample is mainly caused by natural resonance.

Figure 10 shows the absorption effect of C1, C3, C4, C5, C6, and C2 when the thickness D is 1, 2, 3, 4, and 5 mm. As can be seen from Figure 10, C3, C4, C5, and C6 failed to generate effective absorption peaks (less than −10 dB) in the range of 2−18 GHz. It is indicated that the absorption effect of the sample is poor, and only C1 has the effective absorption bandwidth. The reason may be that the corolla-like structure increases its heterogeneity and improves its microwave absorbing property.

As shown in Figure 10a, a maximum absorption peak of −15 dB at 14.02 GHz with an effective bandwidth of 0.87 GHz (13.9−14.77 GHz) was observed when the thickness of the C1 sample was 3 mm. It can be seen that C1 had the best microwave absorbing property among the five samples. In addition, C2 was prepared by $FeCl_3$ complexation of corolla Schiff base C1, and it was found that the microwave absorbing properties of the complex of C1 with Fe^{3+} were improved remarkably. First, when the thickness of the C2 sample is 2 mm, the strongest absorption peak is −36.25 dB at 13.34 GHz and less than −10 dB at 12.72−14.02 GHz. Then, when the sample thickness is 3 mm, it has an effective absorption bandwidth of 2.68 GHz (12.44−15.16 GHz). Finally, when the sample thickness is 4 mm, the effective absorption bandwidth is 1.76 GHz (13.63−15.39 GHz), and the maximum absorption peak is −24.68 dB. It can be seen that the absorption peak moves to a higher frequency with the increase of the thickness.

Reflectivity three-dimensional (3D) plots of C1 and C2 are shown in Figure 11a,b. When the thickness reaches 3.4 mm, the strongest absorption peak is −16.35 dB at 14.43 GHz, and its absorbing bandwidth is 0.72 GHz (14.0−14.72 GHz). There is only one peak in the whole absorbing frequency band. From Figure 11b, when the thickness of the material is 3.8 mm, the maximum reflectivity is −45.07 dB at 14.66 GHz, the absorption peak above −10 dB is 1.71 GHz (13.68−15.39 GHz), and the absorption peak above −20 dB is 0.46 GHz (14.46−14.92 GHz). The peak value of the absorption peak moves to the high frequency with an increase in the thickness. When D = 5 mm, there are double absorption peaks, which shows that C2 has excellent absorbing performance.

$$Z = \left|\frac{Z_{in}}{Z_0}\right| = \left|\sqrt{\frac{\mu_r}{\varepsilon_r}}\tanh\left(j\frac{2\pi fd}{c}\sqrt{\frac{u_r}{\varepsilon_r}}\right)\right| \quad (4)$$

When the impedance matching performance is poor, the electromagnetic wave cannot enter the inner part of the material and be reflected directly from the surface.[43,44] The dielectric matching characteristic is expressed by the Z value,

https://doi.org/10.1021/acsomega.3c02956
ACS Omega 2023, 8, 38885−38894

and the calculation formula is formula 7.[45] When the normalized impedance Z is close to 1, the electromagnetic wave is easier to enter the material.[46,47] According to the formula, the Z values of C1 and C2 are calculated, which are shown in Figure 11c,d. It can be seen from Figure 11c that C1 can reach Z = 1 in the range of 4.97−18 GHz when the thickness is close to 1.85−5 mm, which indicates that the material has good matching performance. With the increase of the sample thickness, the absorption peak can appear at 4.97−18 GHz. It can be seen from Figure 11d that with the increase of thickness, C2 can reach Z = 1 in the range of 1.5−5 mm, and two impedance-matched absorption bands appear with the increase of thickness; this means that the absorption peaks appear at both high and low frequencies when the thickness of the material increases, which is consistent with the 3D absorption map of C2.

4. CONCLUSIONS

Corolla Poly-Schiff bases were synthesized by a block reaction, which were composed of spherical Schiff bases as the "core" and lamella Schiff bases as the "petal." A series of corolla Schiff bases with different morphological characteristics were prepared by adjusting the ratio of the spherical Schiff base and sheet Schiff base. Scanning electron microscopy and electromagnetic parameters show that when the ratio of spherical Schiff bases and lamella Schiff bases is 2:1, the corolla structures are complete. Besides, when the sample thickness reaches 3.4 mm, the strongest absorption peak is −16.35 dB at −14.43 GHz, and the absorption bandwidth is 0.72 GHz (14.0−14.72 GHz). The Schiff base iron complex formed by the doping of the coronoid Schiff base and Fe^{3+} has a maximum absorption value of −45.07 dB when the thickness is 3.8 mm. Dielectric loss mechanisms are dipole polarization, dielectric polarization, and dielectric relaxation, and the magnetic loss is mainly caused by natural resonance. This paper provides a theoretical reference for the in-depth exploration of the Schiff base absorbent.

AUTHOR INFORMATION

Corresponding Author

Aiwen Qin − *Henan Engineering Technology Research Center for Fiber Preparation and Modification, Zhengzhou 450000, P. R. China; College of Materials Engineering, Henan University of Engineering, Zhengzhou 450000, P. R. China*; Email: polymerlj@126.com, lijun@haue.edu.cn

Authors

Jun Li − *Henan Engineering Technology Research Center for Fiber Preparation and Modification, Zhengzhou 450000, P. R. China; College of Materials Engineering, Henan University of Engineering, Zhengzhou 450000, P. R. China*; orcid.org/0009-0000-8375-2125

Yuhang Hua − *College of Materials Engineering, Henan University of Engineering, Zhengzhou 450000, P. R. China*

Qiannan Yuan − *College of Materials Engineering, Henan University of Engineering, Zhengzhou 450000, P. R. China*

Wenqi Gou − *College of Materials Engineering, Henan University of Engineering, Zhengzhou 450000, P. R. China*

Hao Sun − *College of Materials Engineering, Henan University of Engineering, Zhengzhou 450000, P. R. China*

Long Lin − *College of Materials Engineering, Henan University of Engineering, Zhengzhou 450000, P. R. China*

Mengtao Wang − *College of Materials Engineering, Henan University of Engineering, Zhengzhou 450000, P. R. China*

Mingxun Yu − *China North Industries Group, Ji'nan 250031, P. R. China*

Complete contact information is available at: https://pubs.acs.org/10.1021/acsomega.3c02956

Author Contributions

The manuscript was written through contributions of all authors. All authors have given approval to the final version of the manuscript.

Notes

The authors declare no competing financial interest.

ACKNOWLEDGMENTS

This work was supported by the Entrepreneurship Project for College Students in Henan Province (grant nos. 202211517021 and 202211517009) and National Innovation and Entrepreneurship Training Program for College Students (grant no. 202311517004).

REFERENCES

(1) Bao, Y.; Guo, S.; Li, Y.; Jia, Z.; Guan, H.; Lei, D.; Chen, J.; Zhong, B.; Li, Z. Lightweight honeycomb rGO/$TI_3C_2T_x$ Mxene aerogel without magnetic metals toward efficient electromagnetic wave absorption performance. *ACS Appl. Electron. Mater.* **2023**, *5*, 227−239.

(2) Liu, C.; Wu, P.; Chen, S.; Su, Z.; Vishwakarma, S.; Guo, X.; Zheng, Z.; Yu, J.; Wen, S.; Xu, S.; et al. Kill two birds with one stone: multifunctional porous SiOC−Fe_2O_3 composite for li ion energy conversion and electromagnetic wave absorption. *ACS Appl. Electron. Mater.* **2022**, *4*, 6177−6188.

(3) Wang, P.; Li, Z.; Cheng, L.; Ye, F.; Zhang, L. SiC/rGO Core−Shell nanowire as a lightweight, highly efficient gigahertz electromagnetic wave absorber. *ACS Appl. Electron. Mater.* **2020**, *2*, 473−482.

(4) Kong, L.; Yin, X.; Zhang, Y.; Yuan, X.; Li, Q.; Ye, F.; Cheng, L.; Zhang, L. Electromagnetic wave absorption properties of reduced graphene oxide modified by maghemite colloidal nanoparticle clusters. *J. Phys. Chem. C* **2013**, *117*, 19701−19711.

(5) Ren, J.; Lyu, Y.; Liu, Z.; Ahmad, M.; Zhang, Q.; Zhang, B. Microwave absorption performance evaluation of carbonized derivatives of Fe_3O_4@MOF-74 with controllable morphologies. *ACS Appl. Electron. Mater.* **2022**, *4*, 5221−5233.

(6) Han, H.; Lou, Z.; Wang, P.; Wang, Q.; Li, R.; Zhang, Y.; Li, Y. Synthesis of ultralight and porous magnetic g-C_3N_4/g-Carbon foams with excellent electromagnetic wave (EMW) absorption performance and their application as a reinforcing agent for 3D printing EMW absorbers. *Ind. Eng. Chem. Res.* **2020**, *59*, 7633−7645.

(7) Yan, J.; Huang, Y.; Yan, Y.; Ding, L.; Liu, P. High-performance electromagnetic wave absorbers based on two kinds of nickel-based MOF-derived Ni@C microspheres. *ACS Appl. Mater. Interfaces* **2019**, *11*, 40781−40792.

(8) Miao, P.; Yang, J.; Liu, Y.; Xie, H.; Chen, K.-J.; Kong, J. Emerging perovskite electromagnetic wave absorbers from Bi-metal−organic frameworks. *Cryst. Growth Des.* **2020**, *20*, 4818−4826.

(9) Liu, C.; Li, L.; Zhang, X.; Chen, W.-Y.; Zhang, Z. J.; Qin, Y.; Chen, D. Synthesis, characterization of chiral poly(ferrocenyl-schiff base) iron(II) complexes/RGO composites with enhanced microwave absorption properties. *Polymer* **2018**, *150*, 301−310.

(10) Xu, Y.; Li, J.; Ji, H.; Zou, X.; Zhang, J.; Yan, Y. Constructing excellent electromagnetic wave absorber with dielectric-dielectric media based on 3D reduced graphene and Ag(I)-schiff base coordination compounds. *J. Alloys Compd.* **2019**, *781*, 560−570.

(11) De Souza, V. R.; Nunes, G. S.; Rocha, R. C.; Toma, H. E. Spectroscopy, electrochemistry and catalytic properties of ruthenium^{II}

complexes containing thetetradentate schiff base ligand N, N′-bis(7-methyl-2-pyridylmethylene)-1,3- diiminopropane. *Inorg. Chim. Acta* **2003**, *348*, 50−56.
(12) Selwin Joseyphus, R.; Viswanathan, E.; Justin Dhanaraj, C.; Joseph, J. Dielectric properties and conductivity studies of some tetradentate Cobalt(II), Nickel(II), and Copper(II) schiff base complexes [J]. *J. King Saud Univ., Sci.* **2012**, *24*, 233−236.
(13) Chen, Y.; Liu, C.-B.; Gong, Y.-N.; Zhong, J.-M.; Wen, H.-L. Syntheses, crystal structures and antibacterial activities of six cobalt (Π) pyrazole carboxylate complexes with helical character. *Polyhedron* **2012**, *36*, 6−14.
(14) Li, J.; Qi, L.; Yang, L. Multicomponent schiff base/MWCNTs/$FeCl_3$ composite: facile synthesis and strong absorption properties. *Mater. Lett.* **2018**, *213*, 71−74.
(15) Zhao, J.; Xie, Y.; Hu, D.; Guan, D.; Chen, J.; Yu, J.; He, S.; Lü, Y.; Liu, H.; Bao, S.; Wang, L. Phenylenediamine−benzaldehyde schiff base Ag(I) complexes grown on graphene with the intercalated structures for electromagnetic composites. *Synth. Met.* **2015**, *204*, 95−102.
(16) Hassib, H.; Abdel Razik, A. Dielectric properties and ac conduction mechanism communications, for 5,7-dihydroxy-6-formyl-2-methylbenzo-pyran-4one-bis-schiff base. *Solid State Commun.* **2008**, *147*, 345−349.
(17) Courric, S.; Tran, V. H. The electromagnetic properties of blends of poly(p-phenylene-vinylene) derivatives. *Polym. Adv. Technol.* **2000**, *11*, 273−279.
(18) Li, J.; Qi, L.; Li, H. H. Synthesis and dielectric properties of $FeCl_3$/conjugated ploy schiff base composite. *Chin. J. Inorg. Chem.* **2016**, *32*, 96−102.
(19) Li, J.; Qi, L.; Li, H. H. A facile strategy to prepare light-weight PVA membrane based on schiff bases derivative and MWCNTs for electromagnetic wave absorption. *J. Phys. Chem. C* **2016**, *120*, 22865−22872.
(20) Uysal, Ş.; Koc, Z. E. Synthesis and characterization of dendrimeric melamine cored [salen/salophFe (III)] and [Salen/SalophCr (III)] capped complexes and their magnetic behaviors. *J. Hazard. Mater.* **2010**, *175*, 532−539.
(21) Kaya, Í.; Yıldırım, M.; Avcı, A. Synthesis and characterization of fluorescent polyphenol species derived from methyl substituted aminopyridine based schiff bases: the effect of substituent position on optical, electrical, electrochemical, and fluorescence properties. *Synth. Met.* **2010**, *160*, 911−920.
(22) Shao, G.; Shen, X.; Huang, Xiao. Multilevel structural design and heterointerface engineering of a host−guest binary aerogel toward multifunctional broadband microwave absorption. *ACS Mater. Lett.* **2022**, *4*, 1787−1797.
(23) Huang, J.; Gu, H.; Li, N.; Yang, H.; Chen, G.; Zhang, L.; Dong, C.; Guan, H. Polypyrrole/schiff base composite as electromagnetic absorbing material with high and tunable absorption performance. *Molecules.* **2022**, *27*, 6160.
(24) Xu, Y.; Li, J.; Ji, H.; Zou, X.; Zhang, J.; Yan, Y. Constructing excellent electromagnetic wave absorber with dielectricdielectric media based on 3D reduced graphene and Ag(I)-Schiff base coordination compounds. *J. Alloys Compd.* **2019**, *781*, 560−570.
(25) Lou, Z.; Li, Y.; Han, H.; Ma, H.; Wang, L.; Cai, J.; Yang, L.; Yuan, C.; Zou, J. Synthesis of porous 3D Fe/C composites from waste wood with tunable and excellent electromagnetic wave absorption performance. *ACS Sustainable Chem. Eng.* **2018**, *6*, 15598−15607.
(26) Zhao, G.; Lv, H.; Zhou, Y.; Zheng, X.; Wu, C.; Xu, C. Self-assembled sandwich-like MXene-derived nanocomposites for enhanced electromagnetic wave absorption. *ACS Appl. Mater. Interfaces* **2018**, *10*, 42925−42932.
(27) Ghosh, K.; Srivastava, S. K. Fabrication of n-doped reduced graphite oxide/$MnCo_2O_4$ nanocomposites for enhanced microwave absorption performance. *Langmuir* **2021**, *37*, 2213−2226.
(28) Shao, G.; Shen, X.; Huang, X. Multilevel structural design and heterointerface engineering of a host−guest binary aerogel toward multifunctional broadband microwave absorption. *ACS Materials Lett.* **2022**, *4*, 1787−1797.
(29) Huang, J.; Gu, H.; Li, N.; Yang, H.; Chen, G.; Zhang, L.; Dong, C.; Guan, H. Polypyrrole/schiff base composite as electromagnetic absorbing material with high and tunable absorption performance. *Molecules* **2022**, *27*, 6160.
(30) Gao, Q.; Chen, F.; Zhang, J.; Hong, G.; Ni, J.; Wei, X.; Wang, D. The study of novel Fe_3O_4@γ-Fe_2O_3 core/shell nanomaterials with improved properties. *J. Magn. Magn. Mater.* **2009**, *321*, 1052−1057.
(31) Cui, C.; Bai, W.; Jiang, S.; Wang, W.; Ren, E.; Xiao, H.; Zhou, M.; Zhang, J.; Hu, J.; Cheng, C.; Guo, R. FeNi LDH/Loofah sponge-derived magnetic FeNi alloy nanosheet array/porous carbon hybrids with efficient electromagnetic wave absorption. *Ind. Eng. Chem. Res.* **2022**, *61*, 10078−10090.
(32) Peng, H.; Zhang, X.; Yang, H.; Xiong, Z.; Liu, C.; Xie, Y. Fabrication of core-shell nanoporous Carbon@Chiral polyschiff base iron(II) composites for high-performance electromagnetic wave attenuationin the low-frequency. *J. Alloys Compd.* **2021**, *850*, No. 156816.
(33) Huang, Y.; Xie, Y.; Zhao, J.; Yin, X.; Chai, C. Variety of ZIF-8/MXene-based lightweight microwave-absorbing materials: preparation and performances of ZnO/MXene nanocomposites. *J. Phys. Chem. C* **2022**, *126*, 13847−13853.
(34) Nan, H.; Luo, F.; Jia, H.; Deng, H.; Qing, Y.; Huang, Z.; Wang, C.; Chen, Q. Balancing between polarization and conduction loss toward strong electromagnetic wave absorption of hard carbon particles with morphology heterogeneity. *ACS Appl. Mater. Interfaces* **2022**, *14*, 19836−19846.
(35) Liu, C.; Chen, Z.; Xiang, X.; Fang, G.; Wang, Z.; Zhang, Y.; Du, P. Determining the Actual composition of Nb^{5+}−Ni^{2+} codoped barium ferrites to controllably regulate the microwave absorbing properties. *J. Phys. Chem. C* **2022**, *126*, 21800−21809.
(36) Han, S.; Ouyang, B.; Lu, S.; Wu, F.; Xie, A.; Kan, E.; Zeng, H. Carbon nanotubes with tailored amorphous graphitic components for electromagnetic wave absorption. *ACS Appl. Nano Mater.* **2022**, *5*, 16136−16144.
(37) LU, B.; DONG, X. L.; HUANG, H.; et al. Microwave absorption properties of the core/shell-type iron and nickel nanoparticles. *J. Magn. Magn. Mater.* **2008**, *320*, 1106−1111.
(38) Du, X.; Zhang, L.; Guo, C.; Liu, G.; Yuan, H.; Li, Y.; Hu, W. FeCo/Graphene nanocomposites for applications as electromagnetic wave-absorbing materials. *ACS Appl. Nano Mater.* **2022**, *5*, 18730−18741.
(39) Li, F.; Zhan, W.; Zhuang, L.; Zhou, L.; Zhou, M.; Bai, G.; Zhou, A.; Xiao, W.; Yang, X.; Sui, G. Acquirement of strong microwave absorption of $ZnFe_2O_4$@SiO_2@reduced graphene oxide/PVDF composite membranes by regulating crystallization behavior. *J. Phys. Chem. C* **2020**, *124*, 14861−14872.
(40) Huang, Y.; Zhang, N.; Wang, M.; Liu, X.; Zong, M.; Liu, P. Facile synthesis of hollow $Zn_xFe_{3-x}O_4$@Porous MnO_2/rGO conductive network composites for tunable electromagnetic wave absorption. *Ind. Eng. Chem. Res.* **2018**, *57*, 14878−14888.
(41) Xu, D.; Qiao, J.; Wu, N.; Liu, W.; Wang, F.; Lv, L.; Pan, J.; Dong, Y.; Liu, J. Facile synthesis of three-dimensional porous Co/MnO composites derived from bimetal oxides for highly efficient electromagnetic wave absorption. *ACS Sustainable Chem. Eng.* **2019**, *7*, 8687−8695.
(42) Ji, J.; Huang, Y.; Yin, J.; Zhao, X.; Cheng, X.; He, J.; Wang, J.; Li, X.; Liu, J. Electromagnetic wave absorption performance on Fe_3O_4 polycrystalline synthesized by the synergy reduction of ethylene glycol and diethylene glycol. *J. Phys. Chem. C* **2018**, *122*, 3628−3637.
(43) Zhang, X.-F.; Chen, Z.; Feng, Y.; Qiu, J.; Yao, J. Low-temperature transformation of C/SiO_2 nanocomposites to β-SiC with high surface area. *ACS Sustainable Chem. Eng.* **2018**, *6*, 1068−1073.
(44) Lan, D.; Gao, Z.; Zhao, Z.; Kou, K.; Wu, H. Application progress of conductive conjugated polymers in electromagnetic wave absorbing composites. *Compos. Commun.* **2021**, *26*, No. 100767.
(45) Ji, H.; Li, J.; Zhang, J.; Yan, Y. Remarkable microwave absorption performance of ultralight graphene-polyethylene glycol composite aerogels with a very low loading ratio of graphene. *Composites, Part A* **2019**, *123*, 158−169.

https://doi.org/10.1021/acsomega.3c02956
ACS Omega 2023, 8, 38885−38894

(46) Wen, B.; Zhou, Z.; Wang, S.; Zhao, H.; Yang, G.; Wang, J.; Niu, J.; Miao, Y.; Zhang, Z.; Yan, W.; Ding, S. Flexible Cobalt-Embedded Carbon Nanosheet/Carbon Nanofiber Composites for Enhanced Electromagnetic Wave Absorption Performance. *ACS Appl. Nano Mater.* **2023**, *6*, 5404−5413, DOI: 10.1021/acsanm.2c05525.
(47) Liu, Z.; Duan, Y.; Deng, B.; Yang, W.; Han, S.; Hou, L.; Yang, F.; Chen, Z.; Xu, C.; Li, Y. Synthesis of Ultralight N-Rich Porous Graphene Nanosheets Derived from Fluid Catalytic Cracking Slurry and Their Electromagnetic Wave Absorption Properties. *Ind. Eng. Chem. Res.* **2020**, *59*, 8243−8251.

https://doi.org/10.1021/acsomega.3c02956
ACS Omega 2023, 8, 38885−38894